Effect of Water Droplet Growth Dynamics on Electrode Limiting Current in Fuel-Cell Catalyst Layers

John G. Petrovick[1,2], Clayton J. Radke[1], and Adam Z. Weber[2,*]

[1]Department of Chemical and Biomolecular Engineering, University of California, Berkeley

[2]Energy Technologies Area, Lawrence Berkeley National Laboratory

Abstract

Fuel cells are a promising next-generation energy-conversion technology designed to replace internal combustion engines in transportation applications. However, much work remains to optimize them. Operation at high humidities causes liquid water droplet formation on Pt catalyst particles during oxygen reduction, potentially impeding reactant arrival to the reactive electrode. In this work, four different cases of water droplet growth in fuel-cell catalyst layers are considered: pinned and advancing droplets on a bare Pt surface, advancing droplets on a Nafion film, and water-layer growth in carbon nanopores. Transient drop growth is captured with a combination of mass, species mass, and momentum balances, and the subsequent limiting current is determined via oxygen diffusion and Tafel kinetics. Water droplets are found not to be mass-transfer limiting due to the relatively large liquid-gas area compared to the Pt nanoparticle. Mass-transfer-limited behavior is calculated in carbon nanopores.

Introduction

Fuel cells have gradually grown in importance as clean energy-conversion devices. Their relative scalability compared to lithium-ion batteries makes them preferable in many heavy-duty applications, such as in trucks and buses (Cullen et al., 2021). The standard polymer-electrolyte fuel cell (PEFC) operates using the hydrogen-oxidation (HOR) and oxygen-reduction (ORR) reactions, which consume hydrogen and oxygen, respectively, to produce electricity and water as a byproduct. These reactions occur ~~in sequence~~ at the anode and cathode catalyst layers. The two catalyst layers are separated by an ion-conducting membrane that carries protons from the anode to the cathode; the industry standard is Nafion, a perfluorosulfonic acid membrane (Kusoglu and Weber, 2017).

PEFC catalyst layers are complex, heterogeneous structures, (Berlinger et al., 2022; More et al., 2006; Thiele et al., 2011; Weber and Kusoglu, 2014) typically consisting of nm-size platinum (Pt) particles supported on larger carbon particles. The carbon-support particles aggregate into agglomerates that are covered by a thin layer of Nafion (~1-5 nm thick) (Holdcroft, 2013). Solvent drying of the Pt-activated carbon agglomerates into a porous structure forms the catalyst layer, typically ten micrometers thick, with pores ranging from twenty nanometers within agglomerates to up to 100 nm between agglomerates (Holdcroft, 2013; Huang et al., 2017; Suter et al., 2021; Weber and Kusoglu, 2014). Further complexity is added by using carbon particles with varying degrees of internal porosity, such as Vulcan XC-72 (lower porosity) and Ketjen Black (higher porosity) (Holdcroft, 2013; Huang et al., 2017). The final structure of the catalyst layer is critical to device performance because electrons, protons, and reactive gases must have transport pathways to reach the Pt-catalyst surfaces. Carbon acts as an electrical conductor, Nafion is both a proton conductor and a structural support, and non-water

occupied interparticle void pace allows transport of gases. If reactive gases cannot reach active Pt sites, device performance is severely limited.

PEFC performance is normally evaluated by examining voltage losses in polarization curves, or graphs of voltage versus current density. Voltage losses are typically classified as one of three types: kinetic, ohmic, and mass transport (Gerhardt et al., 2021). The mass-transport losses, which are of interest here, are typically attributed to ORR because of oxygen diffusion resistance in the Nafion thin film of the cathode catalyst layer (losses on the hydrogen side are negligible due to the facile nature of the HOR), but other sources are possible (Neyerlin et al., 2007; Sheng et al., 2010; Weber and Kusoglu, 2014). For example, operating at high relative humidity (RH) maximizes the proton conductivity of the polymer membrane and limits ohmic losses (Kusoglu and Weber, 2017). However, water condensation in a high RH environment along with ORR water droplet production partially saturate both the catalyst layer and the adjacent gas diffusion layer (GDL). Significant evidence exists pointing to this phenomenon in GDLs and to the resulting formation of droplets on the exterior surface of the GDL where water exits the GDL (Chen et al., 2005; Chen et al., 2013; Das et al., 2012; Mularczyk et al., 2020; Obeisun et al., 2017; Patel et al., 2019; Wang et al., 2021). Complete aqueous flooding, where gas transport is limited to diffusion through the water-filled pores, can severely restrict gas transport to the catalyst layer. Thus, catalyst-layer flooding is of particular interest given the importance of the catalyst in driving device performance (Li et al., 2008; Nara et al., 2013; Pasaogullari and Wang, 2005; Sabharwal and Secanell, 2022). In general, water management in fuel cells is critical to their overall performance (Andersson et al., 2016; O'Hayre et al., 2016; Vielstich et al., 2003; Weber et al., 2014; Weber and Newman, 2004, 2006).

Nevertheless, few works examine the formation of water droplets in the catalyst layer before two-phase flow commences and cell performance degrades, including nanoscale models of oxygen transport in the catalyst layer (Darling, 2018). ORR produces water as a reaction by-product at the Pt particles in the cathode catalyst layer leading to the generation of water droplets in the catalyst layer (Zhang et al., 2007). Produced droplets subsequently coalesce into two-phase channel flow that restricts oxygen gas from accessing Pt in the catalyst layer and reduces performance. This effect has been previously modeled by assuming Pt sites that are covered by water reduce active surface area (Weber et al., 2014). With minimal experimental evidence of droplet formation and correlation to performance or a transient model simulating droplet growth, it is difficult to know the precise impact that CL-generated water droplets have on cell performance.

Water-droplet formation models (and analogously, bubble-production models) are well-studied in a wide variety of applications ranging from condensation nucleation to examination of bubble growth in electrolyzers, fully-formed droplets adhering to a solid surface, and coalescence of emulsified water or oil droplets in fluid-fluid systems (Angulo et al., 2020; Family and Meakin, 1989; Mohammadi et al., 2012; Nouri-Khorasani et al., 2017; Peeters et al., 2004; Xu et al., 2018; Zhao and Poulikakos, 1996). A key aspect in these models is that droplets form from an external source. With a few exceptions, it is uncommon to grow a droplet from a liquid-producing electrochemical reaction (Perera et al., 2018). However, in fuel cells, water droplets appear because of the water-production reaction: $O_2 + 4H^+ + 4e^- \rightarrow 2H_2O$ inside the droplet at the catalyst surface.

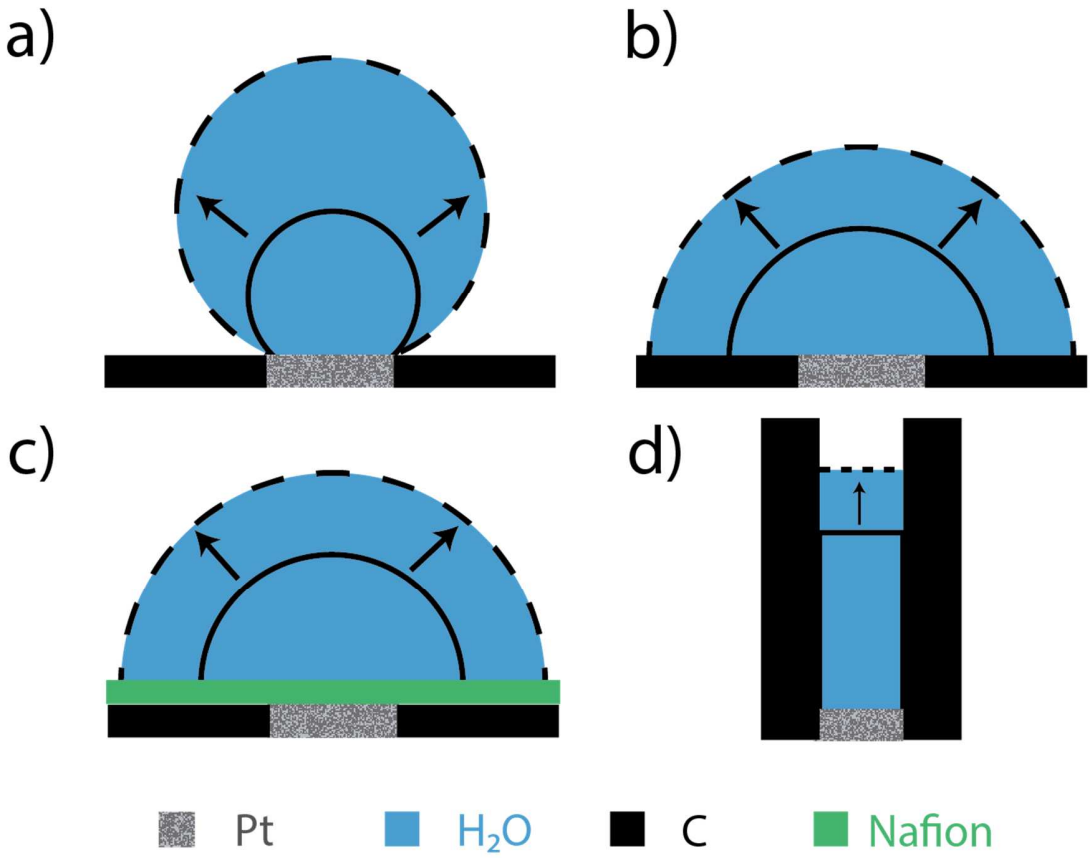

Figure 1: Schematic of the four cases of droplet growth: a) pinned b) advancing c) advancing over Nafion layer d) internal carbon pore.

Large droplet sizes limit oxygen supply both by covering reaction area and by restricting transport through the droplet.

In this work, a computational fluid dynamics model is developed for droplet growth in a cathode catalyst layer. Figure 1 illustrates the four variants considered: drop pinned or advancing drops on a bare Pt surface, growth of an advancing droplet on a Nafion-covered Pt surface, and growth of a water layer on a Pt surface buried at the base of a carbon nanopore. Growth is driven by reactive production of water at the Pt surface and is captured using a moving-mesh framework. Internal droplet convection is described by the Navier-Stokes equation. Fick's

second law captures the transient oxygen diffusion. In all cases, droplet height and current density are evaluated as a function of time for given applied voltages. Finally, the origin and magnitude of system- performance losses, or lack thereof, are addressed.

Model Development

Droplet Growth

There are two major contributions to water-droplet growth in a fuel-cell catalyst layer: growth hydrodynamics and oxygen transport in the growing droplet to the reactive surface. We start with droplet-growth dynamics. A hemispherical water droplet rests on a flat Pt electrode that, in turn, resides on an impermeable carbon surface. Initial drop size is characterized by estimating the remnant drop volume remaining after a previous drop release. The 2D axisymmetric droplet initially extends to the Pt periphery and is surrounded by air at ambient temperature and pressure. As the drop grows due to the ORR, it may either remain pinned at the Pt periphery, as illustrated in Figure 1a, or advance onto the carbon support, as pictured in Figure 1b. Each case is considered separately.

Overall droplet size is controlled by overall mass balance

$$\frac{dm_w}{dt} = \dot{m}_{w,in} = \frac{2M_w}{nF}\int_0^{R_e} i(t,r)2\pi r dr \qquad (1)$$

where m_w is water mass, t is time in seconds, $\dot{m}_{w,in}$ is reaction-produced water mass flowrate, M_w is water molar mass, n is the number of electrons transferred (n = 4 for ORR), F is Faraday's constant, i is ORR current density at the Pt surface, R_e is electrode radius, and r is the radial

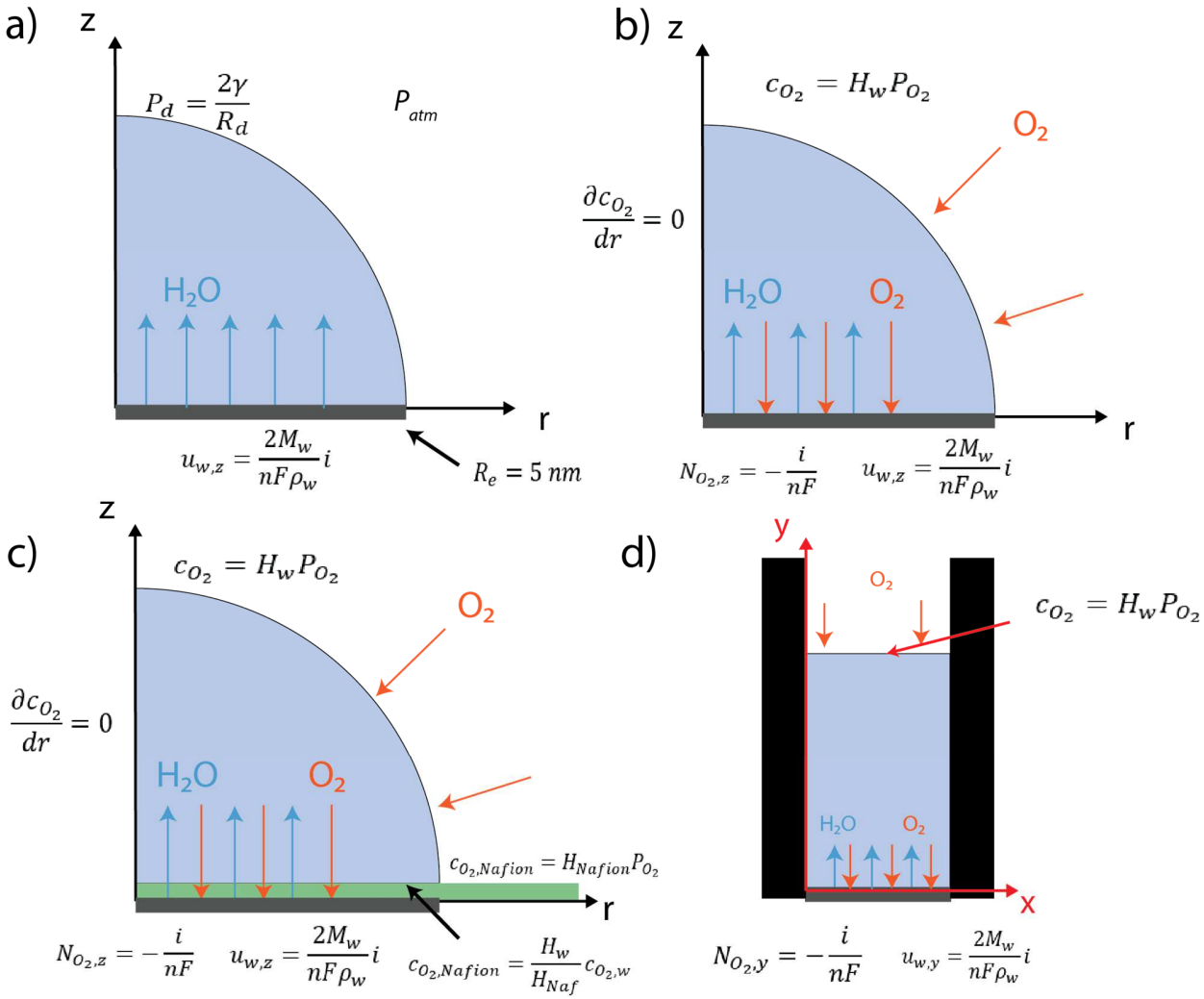

Figure 2: Schematic of boundary conditions for droplet growth. a) diagrams the growth conditions, b-d) oxygen-transport boundary conditions for the bare electrode, Nafion-covered electrode, and internal carbon pore, respectively.

coordinate directed along the abscissa in Figures 2a-c. Dissolved oxygen in the droplet is assumed negligible in the grow hydrodynamics. Current density depends on oxygen arrival to the Pt-catalyst surface, as discussed below. The factor of 2 in the numerator outside the integral in Equation 1 arises from the water to oxygen stoichiometric ratio in the ORR reaction. Evaporation of water into the gas phase is not considered. Inclusion of evaporation, although more accurate, reduces droplet size.

Both momentum and force balances are needed to locate precisely the expanding interface. Momentum balances are imposed for the liquid droplet and the air outside the droplet along with equality of gas and liquid interface velocities (Xu et al., 2018):

$$\rho_w \frac{D\boldsymbol{u_w}}{Dt} = -\nabla P_d + \mu_w \nabla^2 \boldsymbol{u_w} \tag{2}$$

$$\rho_g \frac{D\boldsymbol{u_g}}{Dt} = -\nabla P_g + \mu_g \nabla^2 \boldsymbol{u_g} \tag{3}$$

$$\boldsymbol{u_w}|_{interface} = \boldsymbol{u_g}|_{interface} \tag{4}$$

where ρ_w and ρ_g are the mass density of liquid water and air, μ_w and μ_g are the Newtonian viscosity of liquid water and air, P_d and P_g are the pressure in the liquid water and air, and $\boldsymbol{u_w}$ and $\boldsymbol{u_g}$ are the velocity vectors of water and air in each phase (Bird et al., 2007). Equations 2 and 3 are momentum balances on the water and gas phases, respectively, whereas Equation 4 is the no-slip boundary condition at the interface. The gas phase is stagnant with no external convective flow (i.e., no gas flow occurs over the droplet surface). Symmetry is imposed in the axisymmetric direction. Continuity of total stress is enforced at the interface by the expression:

$$\boldsymbol{n} \cdot \underline{\boldsymbol{\tau_g}} = \boldsymbol{n} \cdot \underline{\boldsymbol{\tau_w}} + \gamma(\nabla_s \cdot \boldsymbol{n})\boldsymbol{n} \tag{5}$$

where $\underline{\boldsymbol{\tau_w}}$ and $\underline{\boldsymbol{\tau_g}}$ are the stress tensors in the water and gas phases, $\boldsymbol{n}$ is the outward unit-normal vector, γ is the surface tension coefficient, and ∇_s is the gradient operator on the droplet surface.

For the pinned drop in Figure 1a, boundary conditions are as follows:

$$\frac{\partial \boldsymbol{u_w}}{\partial r}|_{r=0} = 0$$

$$u_{w,z}(t, r \leq R_e, z = 0) = \frac{2M_w}{nF\rho_w} i(t, r) \tag{6}$$

$$u_{w,z}(t, r > R_e, z = 0) = 0$$

$$\boldsymbol{u_w}(t, r, z = droplet\ edge) \cdot \boldsymbol{n} = 0$$

$$P(t, r, z \to \infty) = P_{atm}$$

where z is the ordinate coordinate in Figure 2a-b directed from the electrode surface. In order, the boundary conditions represent: symmetry at the center axis, water flowrate into the droplet due to chemical reaction at the Pt surface, no reaction at the carbon surface outside the electrode, a water-impermeable liquid-gas interface (i.e., the normal velocity is zero relative to the interface velocity), and a fixed gas pressure equal to atmospheric. In addition, no-slip is imposed inside (liquid) and outside (gas) the droplet on the electrode and carbon surfaces, respectively.

For the initial condition, liquid velocities are zero everywhere, and pressure far away remains atmospheric. Initial droplet radius is set to either that of the reactive surface (R_e = 5 nm) in the pinned droplet case or to double that of the reactive surface (R_e = 10 nm) in the sliding droplet case. These initial conditions are meant to represent the droplet left behind after a previous drop detaches. A precise remnant drop volume is not needed, as we focus on drop limiting current at later growth times. For the advancing droplet, boundary conditions in Equation 6 remain the same, except that slip is allowed. With slip, the droplet advances unhindered along the carbon surface at the initial 90 ° contact angle in accordance with overall mass balance.

Boundary conditions in Equation 6 require specification of the current density at the Pt surface. We utilize a kinetically controlled Tafel expression at the electrode surface where the current depends on the local concentration of oxygen, $c_{O_2}(t, r, z = 0)$:

$$i(t, r) = -i_0 \frac{c_{O_2}(t, r, z = 0)}{c_{O_2,ref}} \exp\left(-\frac{\alpha F}{RT}\eta\right) \tag{7}$$

where i_0 is the exchange current density, $c_{O_2,ref}$ is the oxygen reference α is the symmetry factor, R is the gas constant, T is the temperature, and η is the overpotential (Pant et al., 2019). Table 1 lists values of the parameters. The Tafel equation is accurate over the high overpotentials studied here. Equation 7 demands calculation of the transient oxygen profiles during droplet growth.

Oxygen Transport

Oxygen transport is captured by liquid-phase convection and molecular diffusion:

$$\frac{\partial c_{O_2}}{\partial t} + \boldsymbol{u_w} \cdot \nabla c_{O_2} = D_{O_2} \nabla^2 c_{O_2} \tag{8}$$

where c_{O_2} is the molar concentration of oxygen in the droplet, D_{O_2} is the diffusivity of oxygen in water, and all other symbols are as defined previously (Bird et al., 2007). The water velocity, $\boldsymbol{u_w}$ is determined by Equation 2. It is reasonable to use Fick's law because of the low concentration of oxygen in the water droplet. Boundary conditions for Equation 8 are listed on the droplet schematic in Figure 2b:

$$\frac{\partial c_{O_2}(t, z, r = 0)}{\partial r} = 0$$

$$c_{O_2}(t, r, z = interface) = H_w P_{O_2} \tag{9}$$

$$N_{O_2,z}(t, r \leq R_e)|_{z=0} = \frac{i(t,r)}{nF}$$

$$N_{O_2,z}(t, r > R_e)|_{z=0} = 0$$

where H_w is the Henry's constant for oxygen dissolved in water, $N_{O_2,z}$ is the flux of oxygen in the z direction, and i is local current density. The boundary conditions are symmetry at the center axis, constant concentration at the liquid-gas interface, kinetically controlled current density at the electrode surface from Equations 7 and 9, and zero oxygen flux outside the electrode surface, respectively.

For the Nafion-covered electrode in Figure 2c, all above equations apply, but an additional equation must be added to capture transport of oxygen through the Nafion layer. Fick's second law is again used, but without a convection term:

$$\frac{\partial c_{O_2}}{\partial t} = D_{O_2,Nafion} \nabla^2 c_{O_2} \tag{10}$$

where c_{O_2} is now the oxygen concentration in the Nafion coating per unit film volume and $D_{O_2,Nafion}$ is the diffusivity of oxygen in the Nafion film. All boundary conditions remain the same, but two additional constraints are requisite: one for the water-Nafion interface and a second for the gas-Nafion interface beyond the droplet, as illustrated in Figure 2c.

$$c_{O_2,Nafion}(t, r \geq R_e, z = L) = H_{Nafion} P_{O_2}$$

$$c_{O_2,Nafion}(t, r \leq R_e, z = L) = \frac{H_w}{H_{Nafion}} c_{O_2,w} \tag{11}$$

where H_{Nafion} is Henry's constant for oxygen partitioning in the Nafion phase, L is the thickness of the Nafion layer, and all other variables are defined previously. To remove the effect of differing solubilities in the water and Nafion phases on measured performance, the same solubility was used for both the water and Nafion phases (see Table 1). The initial condition demands phase equilibrium between both the external gas phase and the liquid droplet, and the external gas phase and the Nafion layer, i.e.

$$c_{O_2}(t = 0, r, z) = H_w P_{O_2} \tag{12}$$

Droplet Simulation Description

Equations 1-6 provide accurate description and tracking of the mass of water in the droplet, the interface location and shape, and the internal drop pressure. Equations 7-12 determine the current density as a function of the oxygen transport within the droplet. They are solved simultaneously in COMSOL Multiphysics software via finite elements to produce droplet-growth histories for varying overpotentials. A moving mesh tracks droplet size and interface location. The number of mesh vertices depended on the case studied, with 13062 mesh points for the pinned drop, increasing to 18169 mesh points for the advancing drop, and 48663 mesh points for the advancing drop on Nafion. The ~ 5-nm initial droplet starts with a very dense mesh that is subsequently stretched at each time step based on the solution to the governing equations. Consequently, mesh density decreases with time; longer simulations require increasingly denser initial meshes, restricting the length of performed simulations while obtaining accurate results. This limits the practical size to which we can grow the droplet. Therefore, we limited most simulations to 5 s. Select longer simulations were performed,

however; conclusions did not meaningfully differ. Once the dynamic drop radius is established, the Young-Laplace equation determines the pressure in the spherical droplet, if desired (Angulo et al., 2020):

$$P_d(t) = \frac{2\gamma}{R_d(t)} + P_{atm} \tag{13}$$

where P_d is the time-dependent pressure in the droplet and R_d is the expanding-drop radius. Gravity does not affect drop shape because Bond numbers are small. All physical constants used in the simulations are listed in Table 1. For illustration purposes, initial and advancing-drop contact angle is fixed at 90°. Sensitivity of results to contact angle is weak.

Table 1: Physical Constants

Symbol	**Value**	**Definition**
F	96485 C/mol	Faraday's Constant
n	4	Number of electrons for ORR
M_w	18.02 g/mol	Water Molar Mass
ρ_w	1000 kg/m^3	Water Density
μ_w	1 mPa*s	Water Viscosity
ρ_g	1.2 kg/m^3	Gas density
μ_g	1.7 x 10^{-5} Pa*s	Gas viscosity
γ	72.3 mN/m	Surface tension
P_{atm}	1 atm	Atmospheric Pressure
D_{O_2}	2.42 x 10^{-9} m^2/s (Bergman et al., 2011)	Oxygen Diffusivity in Water
$D_{O_2,Nafion}$	1.04 x 10^{-10} m^2/s (Peron et al., 2010)	Oxygen Diffusivity in Nafion
H_w	1.3 mol/m^3*bar (Sander, 2015)	Henry's Constant of Oxygen in Water
H_{Nafion}	1.3 mol/m^3*bar	Henry's Constant of Oxygen in Nafion
i_0	0.0166 A/m^2	Exchange Current Density
$c_{O_2,ref}$	0.85 mol/m^3 (Pant et al., 2019)	Reference Oxygen Concentration
α	0.479 (Pant et al., 2019)	Transfer Coefficient

R	8.314 J/mol*K	Universal Gas Constant
T	293.15 K	Temperature

Internal Carbon Pore

A schematic for the internal-carbon-pore case is pictured in Figure 2d. A 5-nm radius Pt electrode rests at the bottom of the pore with initially a thin water layer above it. The walls are impermeable, non-reactive carbon. All equations used in the preceding section for the non-Nafion cases apply (Equations 1-9), except 2D Cartesian coordinates, *y* and *x*, are used. Boundary conditions needed are:

$$u_{w,y}(t,x,y=0) = \frac{2}{nFc_w} i(t,x)$$

$$\boldsymbol{u_w}(t,x,y=interface)\cdot\boldsymbol{n} = 0$$

$$P(t,x,y\to\infty) = P_{atm} \tag{14}$$

$$c_{O_2}(t,x,y=interface) = H_w P_{O_2}$$

$$N_{O_2,y}(t,x)|_{y=0} = \frac{i(t,x)}{nF}$$

where c_w is the molar concentration of pure water. The first three boundary conditions in Equation 14 are hydrodynamic: water inlet velocity from the electrochemical reaction, velocity at the extending *y*-interface, and gas pressure far away. The latter two boundary conditions are those for oxygen: concentration of oxygen at the growing liquid-gas interface and oxygen flux at the

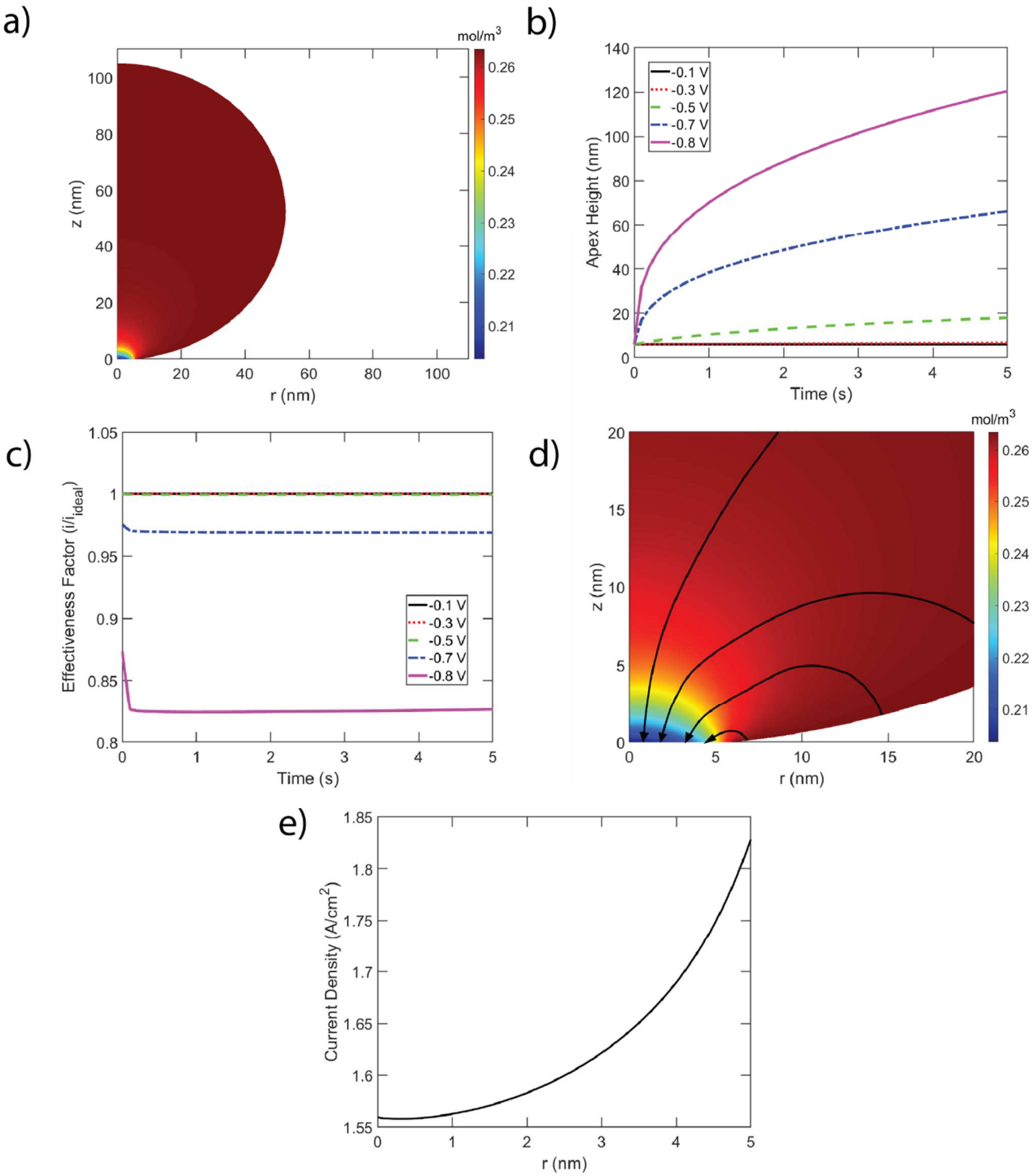

Figure 3: a) Concentration profile of oxygen gas dissolved in the droplet at t = 5 s and an overpotential of -0.8V for a pinned drop. Remaining panels show b) droplet height as a function of time at increasing overpotential, c) effectiveness factor as a function of time and overpotential, d) a concentration profile with streamlines near the electrode surface for the drop in panel a), and e) current distribution along the droplet base at 5 s and an overpotential of -0.8V, respectively.

electrode surface. For the initial condition, velocities are assumed to be zero, and the initial 1-nm water layer is equilibrated with the external gas phase, as in Equation 12. The mesh used consisted of 940 mesh points in this simple 2D geometry. Most simulations were restricted to 1 s due to extremely rapid growth of the water layer in the pore; the only exception involved the determination of the height at which mass-transport limitations occurred ~~(Figure 6d)~~, as described below. In addition, the contact angle was held at 90° for illustration purposes.

Results and Discussion

Bare Pt Electrode

A dissolved oxygen concentration profile is reported in Figure 3a for a pinned droplet growing on a bare Pt electrode at 5 s with $\eta = -0.8\,V$. Oxygen depletion is nearly constant across the electrode except for an increase close to the contact line. Pinning of the droplet to the edge of the electrode surface is clearly demonstrated by examination of the three-phase contact line, which remains at the initial droplet radius of 5 nm and with a contact angle significantly larger than the initially pinned 90°. The droplet apex height at $r = 0$ increases quite rapidly, especially at high overpotential (-0.7 V and higher), as demonstrated by Figure 3b. This dependence is expected due to the use of Tafel kinetics (Equation 7) and the high reaction rates at high overpotential. Figure 3c shows the effectiveness factor as a function of time and overpotential (and therefore droplet size, implicitly). Here current density (per unit Pt area) is normalized by that calculated from the maximum possible concentration of oxygen dissolved in water (i.e., the boundary condition at the drop exterior). These results are unexpected, as the current density does not

appear to decay with time. After the initial decline, a time-independent oxygen boundary layer forms at the droplet base. In other words,

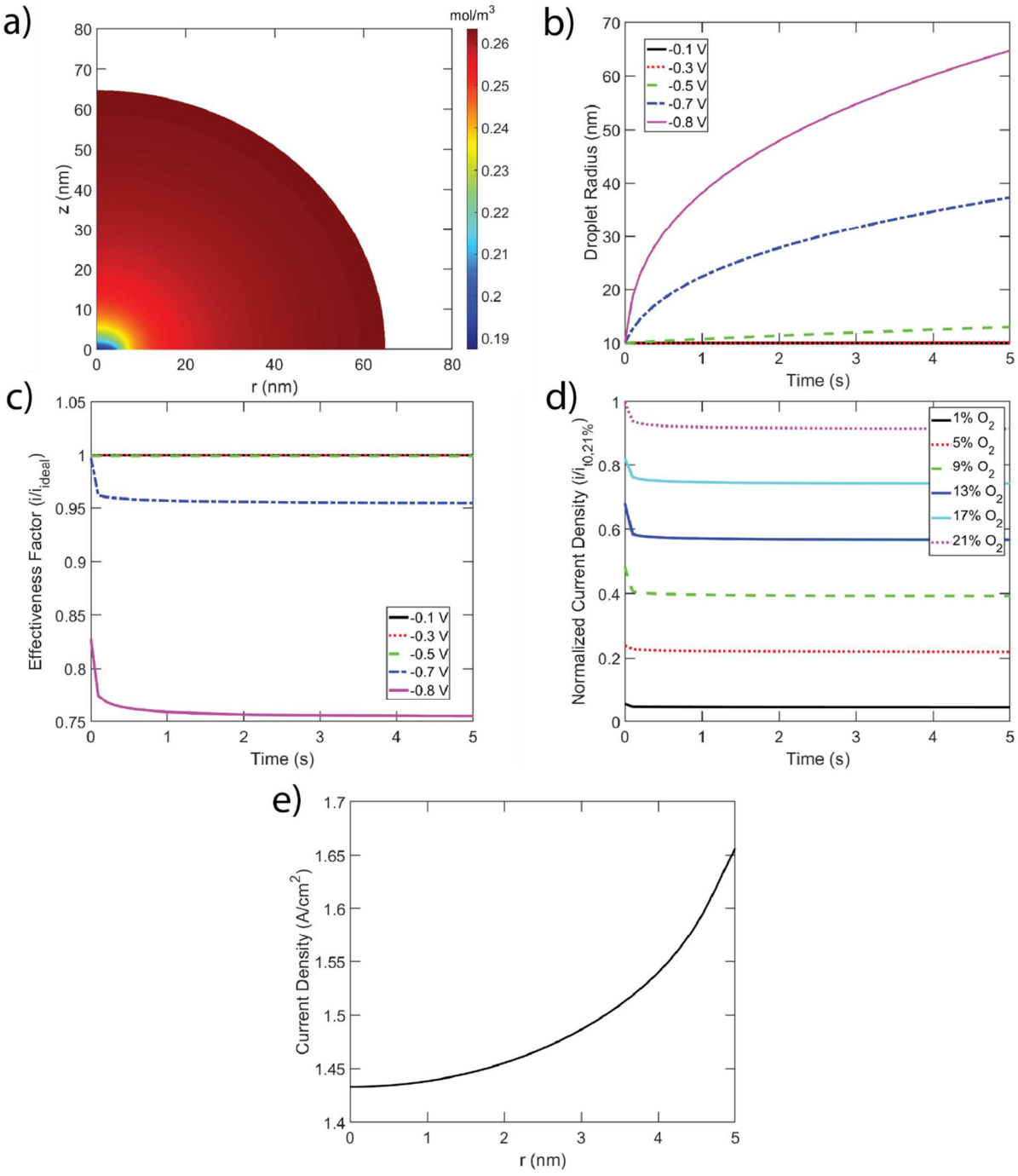

Figure 4: a) Concentration profile of oxygen gas dissolved in the droplet at t = 5 s and an overpotential of -0.8V for an advancing drop. Remaining panels show b) droplet height as a function of time at increasing overpotential, c) effectiveness factor as a function of time and

overpotential, ~~and~~ d) normalized transient current densities for drops exposed to various gas mole percentages relative to 21% oxygen and 1 atm air at -0.8V, and e) current distribution along the droplet base at 5 s and an overpotential of -0.8V, respectively.

current density does not depend on droplet size and mass transport in the droplet is not limiting. By pinning the droplet to the electrode, the shortest diffusion path at the three-phase contact line is maintained throughout the entire simulation, as seen in Figures 3d and e. This is where most of the oxygen enters the drop, as well as where the local current density is highest; the supply majority does not change during the simulation.

The pinned-drop corner is eliminated in Figure 4 by allowing the drop contact line to slide over the carbon-support surface. Accordingly, the water droplet should be more limiting to current-density performance. A sliding-droplet oxygen profile at 5 s with $\eta = -0.8\,V$ is exhibited in Figure 4a. The droplet radius in Figure 4b increases much more slowly compared to the pinned case, as growth is uniform in all directions, although a high overpotential is still critical to significant growth. Nevertheless, effectiveness factor transients again indicate little change with time following an initial decline. The sliding drop does, however, lower the current density from 83% to 75% effectiveness compared to a hinged contact angle but is unchanged as the drop grows. This result remains true even in the most severe limiting case, where in Figure 4d, oxygen concentration in the surrounding gas phase is reduced to as low as 1%. As with the pinned drop, current density is still largest near the electrode radius, as illustrated in Figure 4e. Current density is lower than the pinned case, as expected, due to the lower surface oxygen concentration.

Lack of mass-transfer limitations was unexpected in both the pinned and sliding-drop cases for two reasons. First, we anticipated that water welling up from the surface of the electrode would hinder counter oxygen diffusion. The calculations presented in Figures S1 and

S2 in *Supporting Information*, however, disclose that water velocity is near zero and that pressure is pseudo steady and constant throughout the drop. Section 1.1 of SI establishes that the pertinent Reynolds and

Capillary numbers are both very small. Simple scaling then shows that the drop is pseudo steady with both convected and viscous momentum terms negligible (i.e., $\nabla P_d = 0$). The small Capillary numbers maintain a spherical drop shape undistorted by flow. Thus, the momentum equation describes a spherical drop growing at uniform Laplace equilibrium pressure. Essentially, the flux of water produced at the electrode surface is too small to generate significant pressure-driven flow.

The second reason that mass-transport resistance was expected is the lengthening of the diffusion path due to droplet growth and a concomitant reduction in diffusive-reactant supply to the electrode. However, Section 1.2 of SI establishes that the expanding surface area of the growing drop funnels oxygen to a thin boundary layer adjacent to the electrode disk. Beyond the boundary layer, oxygen concentration is in equilibrium with the gas, as discovered in Figures 3 and 4. Because the boundary-layer Peclét number is small and because the drop growth rate considerably slows, especially at later time, the convected-diffusion equation in the boundary layer is pseudo steady with $\nabla^2 c_{O_2} = 0$. This observation explains the constant concentration boundary layer observed in Figures 3 and 4. Essentially, the surface area of the droplet interface greatly exceeds that of the Pt electrode and funnels oxygen to a point (the electrode). This effect gains in importance as the droplet grows, negating the longer diffusion lengths in a large droplet. As a result, mass-transfer of oxygen is never limiting in these systems. This is similar to the behavior of a microelectrode, where solute transport is not significant outside approximately one

electrode radius from the electrode surface (Petrovick et al., 2022). This is largely due to the geometry of microelectrode systems – an almost identical argument to that made in the case of a growing droplet on a Pt catalyst particle. This effect is explored further in the internal carbon nanopore discussion below.

Nafion-Covered Electrode

We also examined the case of droplet growth with an additional resistive Nafion layer covering the Pt electrode (Cullen et al., 2014). In this case, the droplet grows atop the Nafion layer and

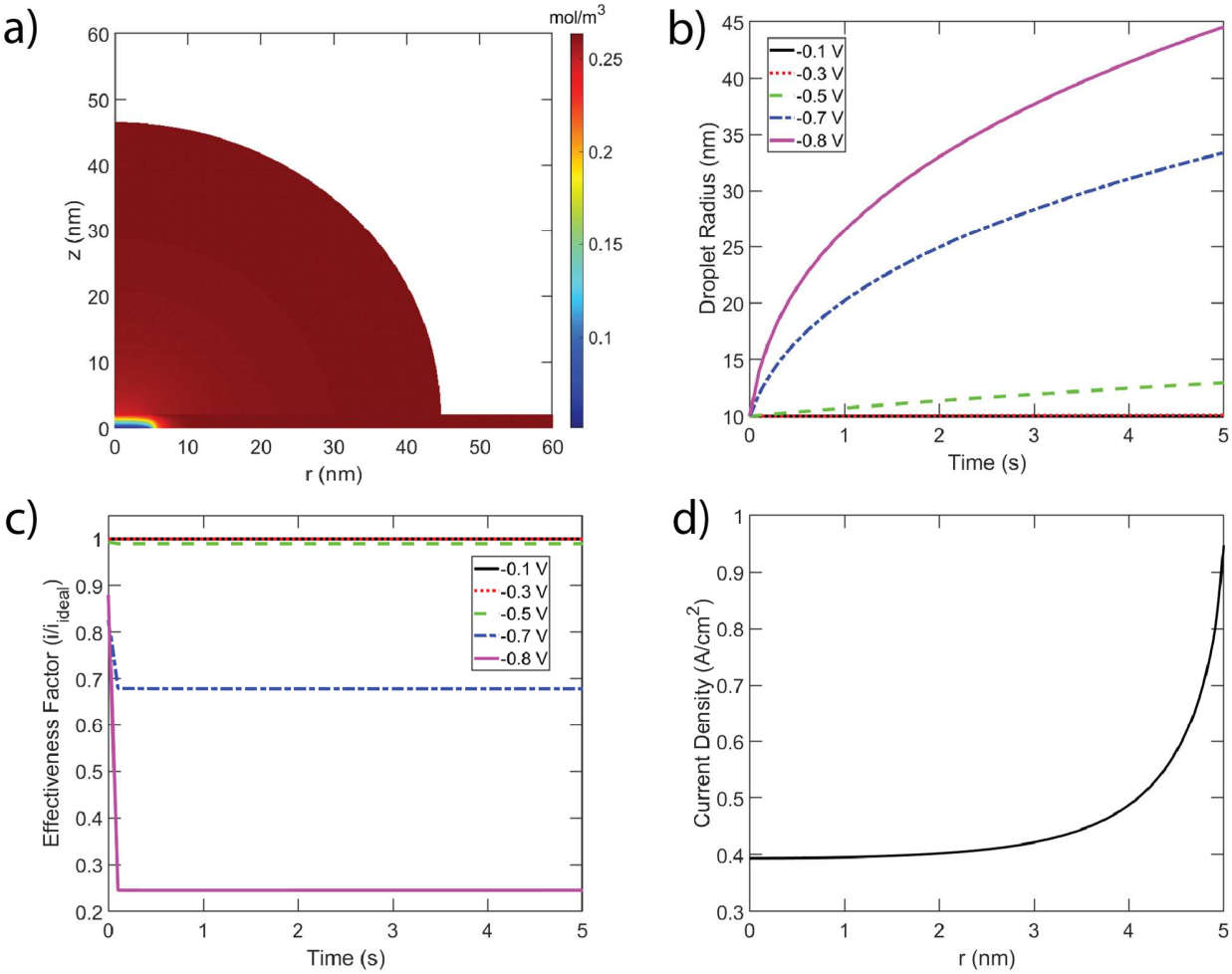

Figure 5: a) Concentration profile of oxygen gas dissolved in the droplet and Nafion layer at t = 5 s and an overpotential of -0.8 V. Remaining panels show b) droplet height as a function of time at increasing overpotential and c) effectiveness factor as a function of time and overpotential,) and d) current distribution along the droplet base at 5 s and an overpotential of -0.8 V, respectively.

slides along the Nafion surface. Contact-line pinning is not likely for the homogeneous, somewhat hydrophilic Nafion surface (Goswami et al., 2008). Water generated at the Pt electrode is assumed to pass directly through the thin Nafion layer with minimal resistance. Values for the diffusivity of oxygen in the droplet and Nafion phases are given in Table 1. The value used for Nafion is that

of liquid-water equilibrated Nafion, about one order of magnitude lower than that in liquid water (Peron et al., 2010).

Figure 5a shows an oxygen concentration profile in a droplet growing over a Nafion-covered electrode at time equals 5 s and at $\eta = -0.8\,V$. Droplet radius is portrayed in Figure 5b as a function of time and overpotential. A time-independent diffusion boundary layer forms in the Nafion layer fed by oxygen funneling similar to the bare Pt electrode in Figure 4. Outside of the boundary layer, the oxygen concentration is uniform in equilibrium with the gas phase, also similar to Figure 4. However, now the boundary-layer thickness is that of the Nafion coating. Section 1.3 of SI establishes that this is due to the order-of-magnitude lower diffusivity of oxygen in Nafion compared to in water. The transient effectiveness factor in Figure 5c confirms this finding. The initial drop in current is sharper because of the steeper oxygen gradient forming in the Nafion layer, indicating worse performance compared to the ideal case. But current, once again, does not change with time. The current distribution at the electrode, demonstrated in Figure 5d, shows a much steeper increase toward the edge of the electrode than either of the Nafion-free cases. This indicates, as expected, that it is more difficult for oxygen to travel to the electrode surface due to the lower diffusivity of oxygen in Nafion, also reflected in the lower normalized current density compared to both preceding cases. Taken together, droplet growth has little impact on electrode performance when a Nafion layer is included.

Internal Carbon Nanopore

The final case is growth of a water layer in an internal carbon nanopore (typically 2-10 nm in diameter), which is functionally water filling a slit (Ramaswamy et al., 2020). Water height as a

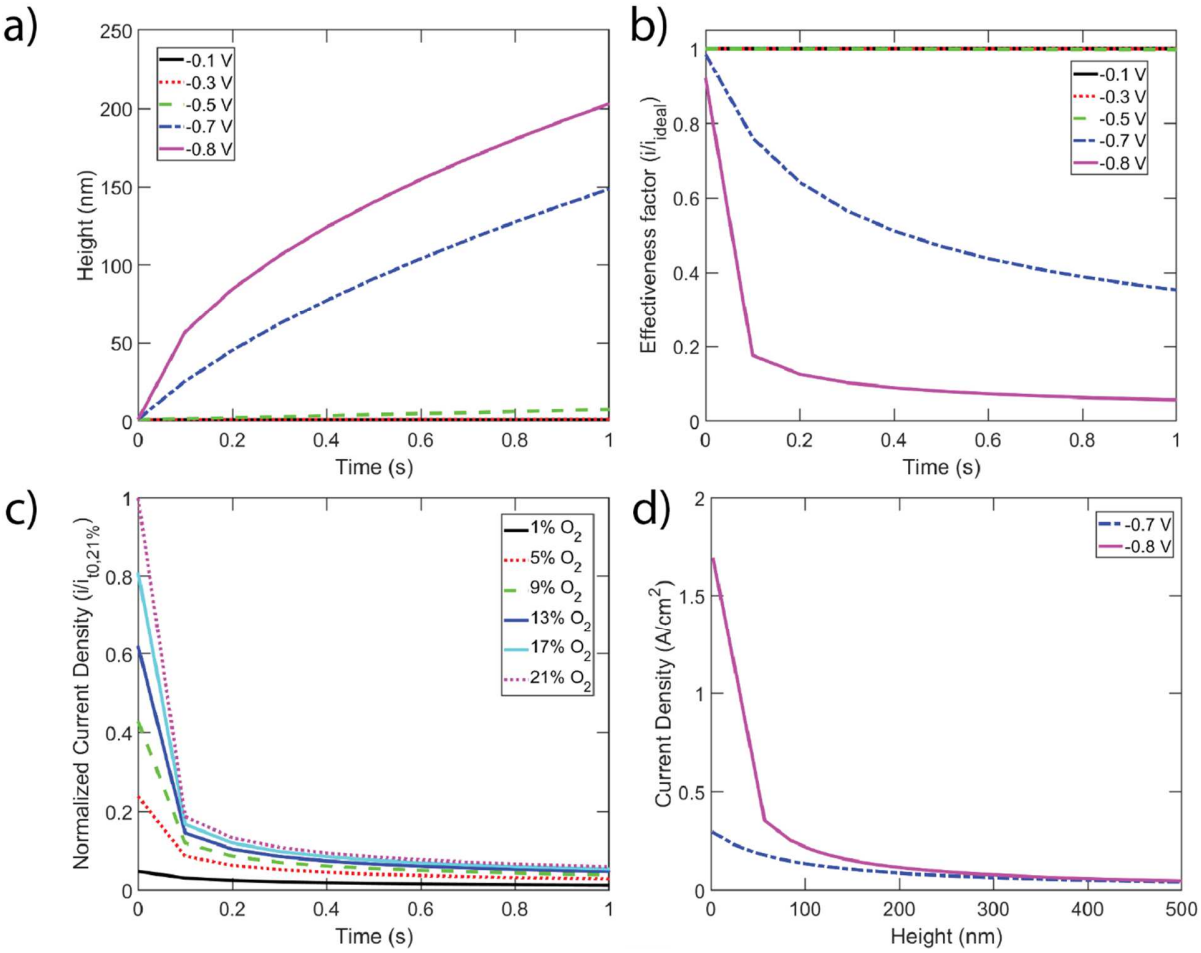

Figure 6: Water-column growth for the internal carbon nanopore. a) and b) height and effectiveness factor, respectively, as a function of time and overpotential c) Normalized current density as a function of oxygen concentration and time at $\eta = -0.8V$ d) Cross-correlation curve indicating the water column height at which the current density curves overlap at high overpotential.

function of time and overpotential is shown in Figure 6a. As in the droplet cases, high overpotential is required to sustain a significant growth rate. However, unlike previous drop-height transients, here high overpotential cases exhibit very similar linear slopes in the height versus time plots following the initial increase. This result implies a similar water production rate

(i.e., current density) under mass-transfer control. Examination of the normalized current density profiles in Figure 6b-c reveals a decrease in effectiveness factor and normalized current density with time, confirming that growth of the water column impacts current density. This too suggests mass-transfer limiting behavior, unlike with growing water droplets.

Mass-transfer limitation is also confirmed in Figure 6d where current density is plotted versus water height for two high overpotentials. At h ~ 300 nm, current density becomes potential-independent indicating that oxygen mass transport through the water column is fully limiting. It is unlikely, however, that actual carbon nanopores extend over such length scales (Holdcroft, 2013). Accordingly, flooding of actual carbon nanopores with water is unlikely to impact measured current densities beyond an initial drop in effectiveness factor.

To confirm that oxygen funneling is the reason that nanopores experience mass-transfer limitations at larger filling heights whereas droplets do not, the example nanopore was widened while keeping the reactive Pt area the same size, i.e., by adding non-reactive carbon surfaces outside the Pt surface at the bottom of the pore. Figure 7a displays a schematic of the widened nanopore. Current density as a function of time for the different pore widths (seen in legend) is captured in Figure 7b. Tripling of the column width leads to a nearly three times higher current density at the same time. To eliminate the impact of different water heights at different times, oxygen concentration at the surface is plotted against water height in Figure 7c for the different column widths. At the same height, a three-fold increase in width causes a two-fold increase in concentration, which leads directly to the higher current densities seen in Figure 7b. A substantial increase in current commences for a relatively small change in pore width. We ascribe this increase to the funneling effect: the large surface area at the liquid-gas interface

directs all the oxygen to a smaller reactive Pt area, which in turn leads to a higher local oxygen concentration and therefore a higher current (Darling, 2018).

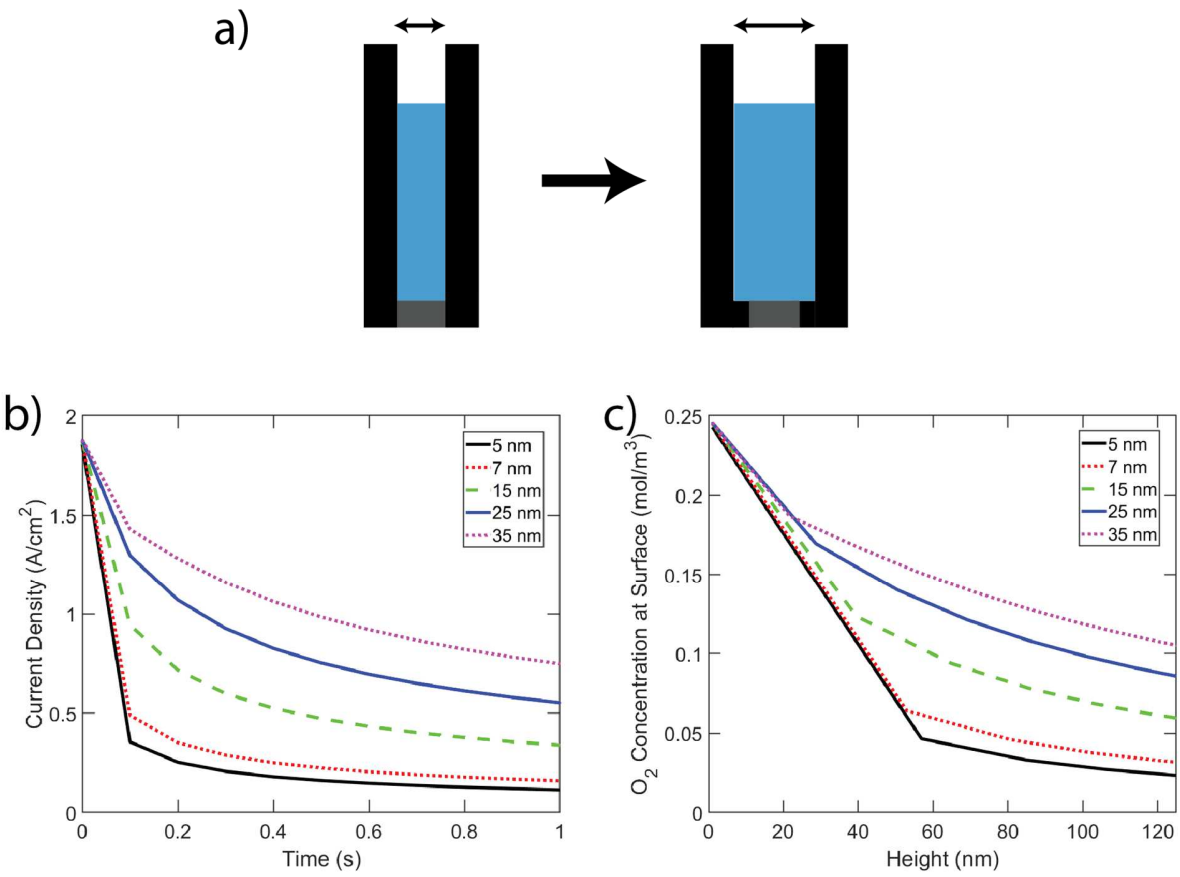

Figure 7: a) Schematic of widening of the nanopore. b) Current density as a function of time and pore width. c) Oxygen concentration at the electrode surface as a function of water column height for several different pore widths.

Reactant funneling is the same reason why droplets do not exhibit transport limiting behavior, as reflected in Figures 3 and 4 (see *Supporting Information* Section 1.2). It is, therefore, unlikely that local water-droplet formation is mass-transfer limiting in current catalyst-layer designs. However, we do not address droplet coalescence here. Coalescence into

continuous water channels does impede gas flow by occupying pore space that otherwise would be gas occupied. Thus, although not considered here, some lowering of system efficiency is possible. It is noteworthy that Sabharwal et al. argue that catalyst-layer flooding, although commonly believed to cause large performance losses, is not as limiting as originally assumed (Sabharwal and Secanell, 2022).

Conclusions

Four cases of water droplet growth in fuel-cell catalyst layers were examined for possible mass-transfer limitations including: bare Pt electrodes with and without droplet slip, Nafion-covered electrodes, and internal carbon pores. Transient mass and momentum balances were solved simultaneously with oxygen species transport in an axisymmetric geometry by finite elements. We find that growth of water droplets is never transport limiting in traditional catalyst layers. For droplet growth on Pt electrodes, the expanding liquid-gas interface funnels oxygen diffusion to the smaller ORR surface overcoming drop-volume growth. Oxygen supply is large enough that the reacting electrode cannot consume the oxygen inflow leading to lack of mass transport limitations. In the case of internal carbon pores, mass-transport limitations exist, but only at pore lengths larger than the size of the pores typically found in fuel-cell catalyst layers. Lack of drop-growth mass-transfer limitations is an important result for fuel-cell optimization, as design changes performed to minimize droplet growth and flooding may not be necessary.

Acknowledgements

The authors thank Drs. Arthur Dizon and Mayank Sabharwal for helpful discussions and assistance using COMSOL. This work was performed under the Million Mile Fuel Cell Truck (M2FCT) Consortium (https://millionmilefuelcelltruck.org), technology manager Greg Kleen, U.S. Department of Energy, Office of Energy Efficiency and Renewable Energy, Hydrogen and Fuel Cell Technologies Office: Contract number DE-AC02-05CH11231.

References

Andersson, M., Beale, S.B., Espinoza, M., Wu, Z., Lehnert, W., 2016. A review of cell-scale multiphase flow modeling, including water management, in polymer electrolyte fuel cells. Applied Energy 180, 757-778.

Angulo, A., van der Linde, P., Gardeniers, H., Modestino, M., Fernández Rivas, D., 2020. Influence of Bubbles on the Energy Conversion Efficiency of Electrochemical Reactors. Joule 4, 555-579.

Bergman, T.L., Lavine, A.S., Incropera, F.P., Dewitt, D.P., 2011. Fundamentals of Heat and Mass Transfer, Seventh ed. John Wiley & Sons, Inc., Hoboken, NJ.

Berlinger, S.A., Chowdhury, A., Van Cleve, T., He, A., Dagan, N., Neyerlin, K.C., McCloskey, B.D., Radke, C.J., Weber, A.Z., 2022. Impact of Platinum Primary Particle Loading on Fuel Cell Performance: Insights from Catalyst/Ionomer Ink Interactions. ACS Appl Mater Interfaces 14, 36731-36740.

Bird, R.B., Stewart, W.E., Lightfoot, E.N., 2007. Transport Phenomena, rev. 2nd ed. John Wiley & Sons, Inc., New York.

Chen, K.S., Hickner, M.A., Noble, D.R., 2005. Simplified models for predicting the onset of liquid water droplet instability at the gas diffusion layer/gas flow channel interface. International Journal of Energy Research 29, 1113-1132.

Chen, L., He, Y.-L., Tao, W.-Q., 2013. Effects of surface microstructures of gas diffusion layer on water droplet dynamic behaviors in a micro gas channel of proton exchange membrane fuel cells. International Journal of Heat and Mass Transfer 60, 252-262.

Cullen, D.A., Koestner, R., Kukreja, R.S., Liu, Z.Y., Minko, S., Trotsenko, O., Tokarev, A., Guetaz, L., Meyer, H.M., Parish, C.M., More, K.L., 2014. Imaging and Microanalysis of Thin Ionomer Layers by Scanning Transmission Electron Microscopy. Journal of The Electrochemical Society 161, F1111-F1117.

Cullen, D.A., Neyerlin, K.C., Ahluwalia, R.K., Mukundan, R., More, K.L., Borup, R.L., Weber, A.Z., Myers, D.J., Kusoglu, A., 2021. New roads and challenges for fuel cells in heavy-duty transportation. Nature Energy 6, 462-474.

Darling, R.M., 2018. A Hierarchical Model for Oxygen Transport in Agglomerates in the Cathode Catalyst Layer of a Polymer-Electrolyte Fuel Cell. Journal of The Electrochemical Society 165, F571-F580.

Das, P.K., Grippin, A., Kwong, A., Weber, A.Z., 2012. Liquid-Water-Droplet Adhesion-Force Measurements on Fresh and Aged Fuel-Cell Gas-Diffusion Layers. Journal of The Electrochemical Society 159, B489-B496.

Family, F., Meakin, P., 1989. Kinetics of droplet growth processes: Simulations, theory, and experiments. Phys Rev A Gen Phys 40, 3836-3854.

Gerhardt, M.R., Pant, L.M., Bui, J.C., Crothers, A.R., Ehlinger, V.M., Fornaciari, J.C., Liu, J., Weber, A.Z., 2021. Method—Practices and Pitfalls in Voltage Breakdown Analysis of Electrochemical Energy-Conversion Systems. Journal of The Electrochemical Society 168.

Goswami, S., Klaus, S., Benziger, J., 2008. Wetting and absorption of water drops on Nafion films. Langmuir 24, 8627-8633.

Holdcroft, S., 2013. Fuel Cell Catalyst Layers: A Polymer Science Perspective. Chemistry of Materials 26, 381-393.

Huang, J., Li, Z., Zhang, J., 2017. Review of characterization and modeling of polymer electrolyte fuel cell catalyst layer: The blessing and curse of ionomer. Frontiers in Energy 11, 334-364.
Kusoglu, A., Weber, A.Z., 2017. New Insights into Perfluorinated Sulfonic-Acid Ionomers. Chem Rev 117, 987-1104.
Li, H., Tang, Y., Wang, Z., Shi, Z., Wu, S., Song, D., Zhang, J., Fatih, K., Zhang, J., Wang, H., Liu, Z., Abouatallah, R., Mazza, A., 2008. A review of water flooding issues in the proton exchange membrane fuel cell. Journal of Power Sources 178, 103-117.
Mohammadi, M., Shahhosseini, S., Bayat, M., 2012. Direct numerical simulation of water droplet coalescence in the oil. International Journal of Heat and Fluid Flow 36, 58-71.
More, K.L., Borup, R.L., Reeves, K.S., 2006. Identifying Contributing Degradation Phenomena in PEM Fuel Cell Membrane Electrode Assemblies Via Electron Microscopy. ECS Transactions 3, 717-733.
Mularczyk, A., Lin, Q., Blunt, M.J., Lamibrac, A., Marone, F., Schmidt, T.J., Büchi, F.N., Eller, J., 2020. Droplet and Percolation Network Interactions in a Fuel Cell Gas Diffusion Layer. Journal of The Electrochemical Society 167.
Nara, H., Momma, T., Osaka, T., 2013. Impedance analysis of the effect of flooding in the cathode catalyst layer of the polymer electrolyte fuel cell. Electrochimica Acta 113, 720-729.
Neyerlin, K.C., Gu, W.B., Jorne, J., Gasteiger, H.A., 2007. Study of the exchange current density for the hydrogen oxidation and evolution reactions. Journal of the Electrochemical Society 154, B631-B635.
Nouri-Khorasani, A., Tabu Ojong, E., Smolinka, T., Wilkinson, D.P., 2017. Model of oxygen bubbles and performance impact in the porous transport layer of PEM water electrolysis cells. International Journal of Hydrogen Energy 42, 28665-28680.
O'Hayre, R., Cha, S.-W., Colella, W.G., Prinz, F.B., 2016. Chapter 6: Fuel Cell Modeling, Fuel Cell Fundamentals. John Wiley & Sons, Hoboken, New Jersey, pp. 203-236.
Obeisun, O.A., Finegan, D.P., Engebretsen, E., Robinson, J.B., Taiwo, O.O., Hinds, G., Shearing, P.R., Brett, D.J.L., 2017. Ex-situ characterisation of water droplet dynamics on the surface of a fuel cell gas diffusion layer through wettability analysis and thermal characterisation. International Journal of Hydrogen Energy 42, 4404-4414.
Pant, L.M., Gerhardt, M.R., Macauley, N., Mukundan, R., Borup, R.L., Weber, A.Z., 2019. Along-the-channel modeling and analysis of PEFCs at low stoichiometry: Development of a 1+2D model. Electrochimica Acta 326.
Pasaogullari, U., Wang, C.Y., 2005. Two-phase modeling and flooding prediction of polymer electrolyte fuel cells. Journal of the Electrochemical Society 152, A380-A390.
Patel, V., Battrell, L., Anderson, R., Zhu, N., Zhang, L., 2019. Investigating effect of different gas diffusion layers on water droplet characteristics for proton exchange membrane (PEM) fuel cells. International Journal of Hydrogen Energy 44, 18340-18350.
Peeters, P., Pieterse, G., van Dongen, M.E.H., 2004. Multi-component droplet growth. II. A theoretical model. Physics of Fluids 16, 2575-2586.
Perera, R.T., Arcadia, C.E., Rosenstein, J.K., 2018. Probing the nucleation, growth, and evolution of hydrogen nanobubbles at single catalytic sites. Electrochimica Acta 283, 1773-1778.
Peron, J., Mani, A., Zhao, X., Edwards, D., Adachi, M., Soboleva, T., Shi, Z., Xie, Z., Navessin, T., Holdcroft, S., 2010. Properties of Nafion® NR-211 membranes for PEMFCs. Journal of Membrane Science 356, 44-51.

Petrovick, J.G., Radke, C.J., Weber, A.Z., 2022. Gas Mass-Transport Coefficients in Ionomer Membranes Using a Microelectrode. ACS Meas Sci Au 2, 208-218.
Ramaswamy, N., Gu, W., Ziegelbauer, J.M., Kumaraguru, S., 2020. Carbon Support Microstructure Impact on High Current Density Transport Resistances in PEMFC Cathode. Journal of The Electrochemical Society 167.
Sabharwal, M., Secanell, M., 2022. Understanding the effect of porosity and pore size distribution on low loading catalyst layers. Electrochimica Acta 419.
Sander, R., 2015. Compilation of Henry's law constants (version 4.0) for water as solvent. Atmospheric Chemistry and Physics 15, 4399-4981.
Sheng, W.C., Gasteiger, H.A., Shao-Horn, Y., 2010. Hydrogen Oxidation and Evolution Reaction Kinetics on Platinum: Acid vs Alkaline Electrolytes. Journal of the Electrochemical Society 157, B1529-B1536.
Suter, T.A.M., Smith, K., Hack, J., Rasha, L., Rana, Z., Angel, G.M.A., Shearing, P.R., Miller, T.S., Brett, D.J.L., 2021. Engineering Catalyst Layers for Next-Generation Polymer Electrolyte Fuel Cells: A Review of Design, Materials, and Methods. Advanced Energy Materials 11.
Thiele, S., Zengerle, R., Ziegler, C., 2011. Nano-morphology of a polymer electrolyte fuel cell catalyst layer—imaging, reconstruction and analysis. Nano Research 4, 849-860.
Vielstich, W., Lamm, A., Gasteiger, H.A., 2003. Handbook of Fuel Cells: Fundamentals, Technology, and Applications. John Wiley & Sons, Chichester, England.
Wang, Y., Wang, X., Wang, X., Liu, T., Zhu, T., Liu, S., Qin, Y., 2021. Droplet dynamic characteristics on PEM fuel cell cathode gas diffusion layer with gradient pore size distribution. Renewable Energy 178, 864-874.
Weber, A.Z., Borup, R.L., Darling, R.M., Das, P.K., Dursch, T.J., Gu, W., Harvey, D., Kusoglu, A., Litster, S., Mench, M.M., Mukundan, R., Owejan, J.P., Pharoah, J.G., Secanell, M., Zenyuk, I.V., 2014. A Critical Review of Modeling Transport Phenomena in Polymer-Electrolyte Fuel Cells. Journal of The Electrochemical Society 161, F1254-F1299.
Weber, A.Z., Kusoglu, A., 2014. Unexplained transport resistances for low-loaded fuel-cell catalyst layers. J. Mater. Chem. A 2, 17207-17211.
Weber, A.Z., Newman, J., 2004. Modeling Transport in Polymer-Electrolyte Fuel Cells. Chem Rev 104, 4679-4726.
Weber, A.Z., Newman, J., 2006. Coupled thermal and water management in polymer electrolyte fuel cells. Journal of the Electrochemical Society 153, A2205-A2214.
Xu, Z., Zhang, L., Wilke, K., Wang, E.N., 2018. Multiscale Dynamic Growth and Energy Transport of Droplets during Condensation. Langmuir 34, 9085-9095.
Zhang, F.-Y., Spernjak, D., Prasad, A.K., Advani, S.G., 2007. In Situ Characterization of the Catalyst Layer in a Polymer Electrolyte Membrane Fuel Cell. Journal of The Electrochemical Society 154, B1152.
Zhao, Z., Poulikakos, D., 1996. Heat transfer and fluid dynamics during the collision of a liquid droplet on a substrate,, I. Modeling. International Journal of Heat and Mass Transfer 39, 2771-2789.

Symbols

A: area

A_e: electrode area

c_{O_2}: oxygen concentration

c_w: liquid water concentration

c_e: equilibrium oxygen concentration

$c_{O_2,ref}$: oxygen reference concentration

$Ca = \mu_w u_{char}/2\gamma$: Capillary number

D_{O_2}: oxygen diffusivity in water

$D_{O_2,Nafion}$: oxygen diffusivity in Nafion

F: Faraday's constant

~~F_f: frictional forces term~~

H: pore column height

H_w: Henry's constant for oxygen in water

H_{Nafion}: Henry's constant for oxygen in Nafion

i: current density

i_0: exchange current density

L: Nafion thickness

m_w: mass of water

$\dot{m}_{w,in}$: water flowrate in

M_w: water molar mass

n: number of electrons

$\boldsymbol{n}$: normal vector

$N_{O_2,z}$: oxygen flux in z direction

N_w: Water flux

P_{atm}: atmospheric pressure

P_d: droplet pressure

$Re = \frac{\rho_w u_{char} R_e}{\mu_w}$: Reynolds number

R: universal gas constant

R_d: droplet radius

R_e: electrode radius

R_w: oxygen resistance in water phase

R_{Naf}: oxygen resistance in Nafion phase

r: radial coordinate

S: droplet surface area

t: time

t_{char}: characteristic time

t_{diff}: characteristic time, diffusion

t_{growth}: characteristic time, droplet growth

T: temperature

$\boldsymbol{u_w}$: water velocity vector

$\boldsymbol{u_g}$: gas velocity vector

V: droplet volume

z: axial coordinate

Greek Symbols

α: transfer coefficient

β: coefficient defined in Equation S3

γ: surface tension

δ: mass-transfer boundary-layer thickness

ρ_w: water density

μ_w: water viscosity

μ_g: gas viscosity

$\underline{\boldsymbol{\tau_g}}$: stress tensor, gas phase

$\underline{\boldsymbol{\tau_w}}$: stress tensor, water phase

∇: gradient operator

∇_S: surface gradient operator

η: overpotential

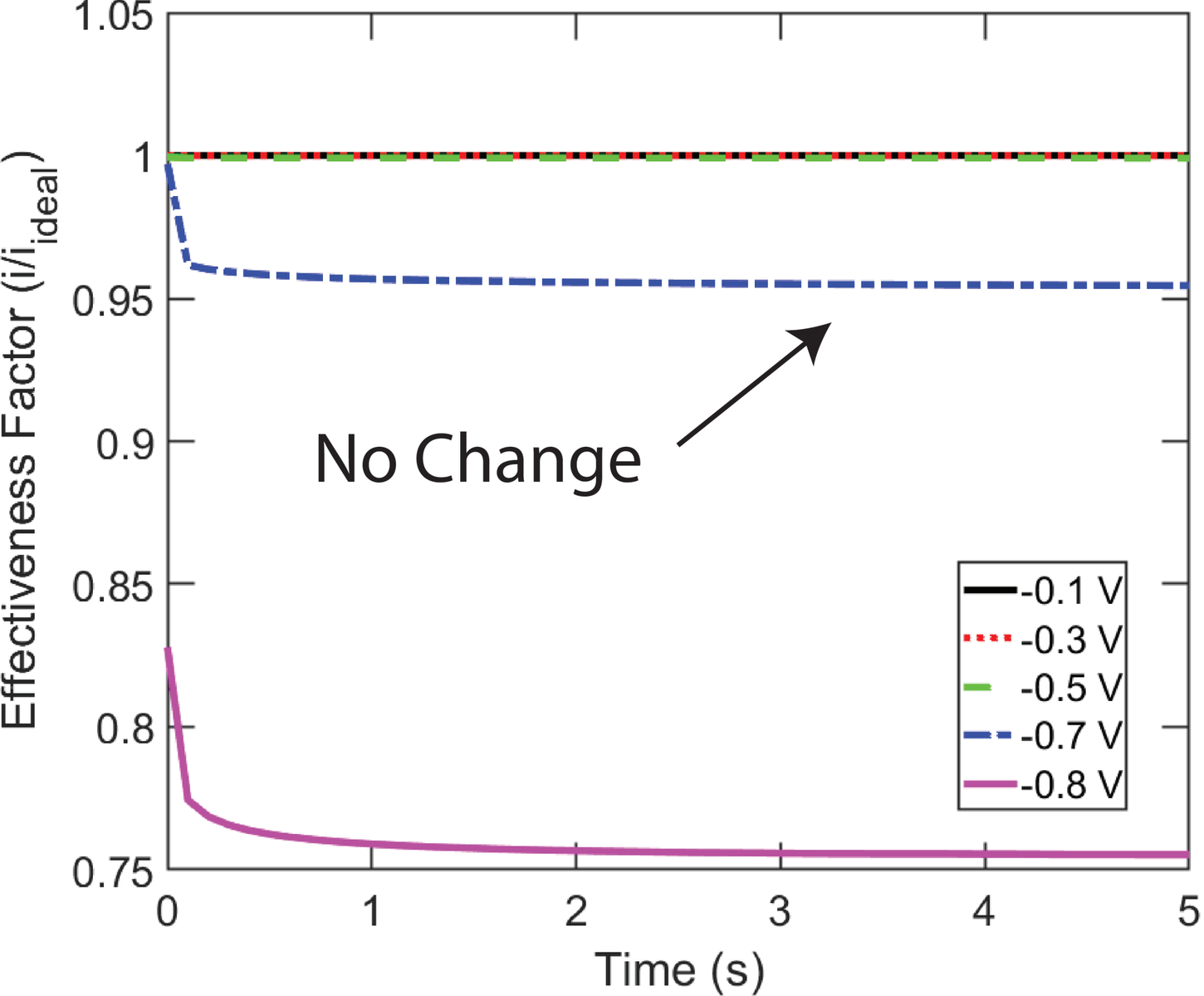
Effectiveness Factor (i/i_ideal)
1.05
1
0.95
0.9
0.85
0.8
0.75
0
1
2
3
4
5
Time (s)
No Change
-0.1 V
-0.3 V
-0.5 V
-0.7 V
-0.8 V

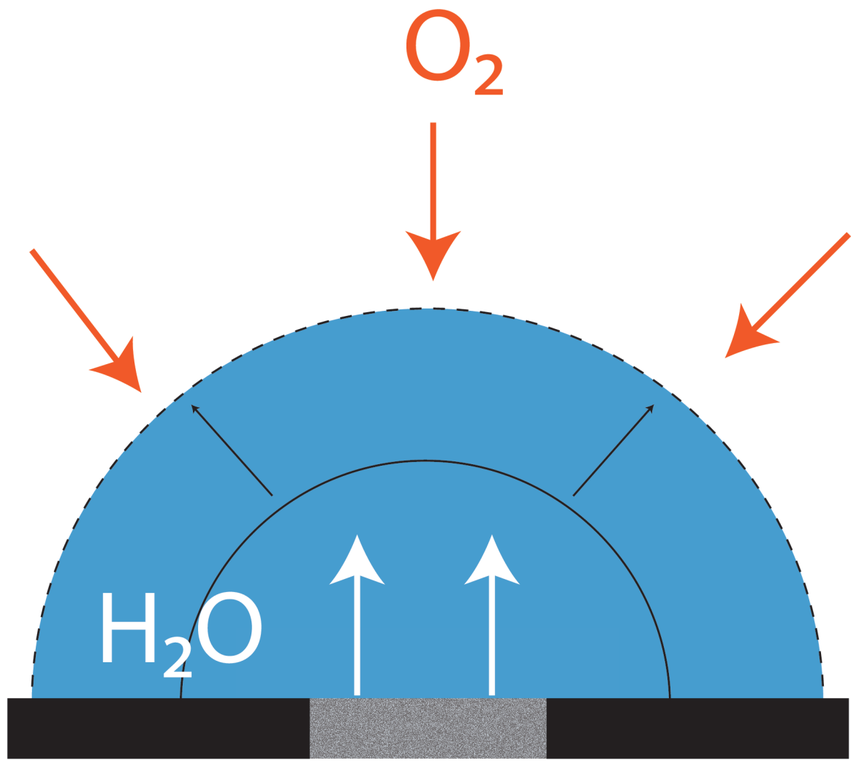
O2
H2O